BEILSTEIN ARCHIVES

This open access document is posted as a preprint in the Beilstein Archives at https://doi.org/10.3762/bxiv.2024.50.v1 and is considered to be an early communication for feedback before peer review. Before citing this document, please check if a final, peer-reviewed version has been published.

This document is not formatted, has not undergone copyediting or typesetting, and may contain errors, unsubstantiated scientific claims or preliminary data.

Preprint Title	Annealing Effects on ZrO_2 Thin Films: Characterization and Gas Sensing Applications
Authors	Carolina Bohórquez, Jorge L. Vazquez-Arce, Ana K. Cuentas-Gallegos and Hugo Tiznado
Publication Date	22 Juli 2024
Article Type	Full Research Paper
ORCID® iDs	Carolina Bohórquez - https://orcid.org/0000-0001-9687-7357; Jorge L. Vazquez-Arce - https://orcid.org/0000-0003-3651-3193; Ana K. Cuentas-Gallegos - https://orcid.org/0000-0003-4516-8889

License and Terms: This document is copyright 2024 the Author(s); licensee Beilstein-Institut.

This is an open access work under the terms of the Creative Commons Attribution License (https://creativecommons.org/licenses/by/4.0). Please note that the reuse, redistribution and reproduction in particular requires that the author(s) and source are credited and that individual graphics may be subject to special legal provisions.
The license is subject to the Beilstein Archives terms and conditions: https://www.beilstein-archives.org/xiv/terms.
The definitive version of this work can be found at https://doi.org/10.3762/bxiv.2024.50.v1

Annealing Effects on ZrO_2 Thin Films: Characterization and Gas Sensing Applications

Carolina Bohórquez[*1], Jorge Vazquez[‡2], Ana Karina Cuentas Gallegos[‡1], Hugo Tiznado[‡1]

[1]Universidad Nacional Autónoma de México, Centro de Nanociencias y Nanotecnología, Km 107 Carretera Tijuana-Ensenada s/n B.C. C.P. 22800 México.
[2]Institute for Metallic Materials, Leibniz Institute for Solid State and Materials Research, Helmholtzstraße 20, 01069 Dresden, Germany

Email: Carolina Bohórquez Martínez – bohormar@ens.cnyn.unam.mx

* Corresponding author

‡ Equal contributors

Abstract

This study investigates the effects of annealing on the structural, optical, and gas-sensing properties of ZrO_2 thin films deposited by atomic layer deposition (ALD). The films were annealed in a nitrogen atmosphere at 700, 800, and 900 °C. Surface morphology, chemical composition, optical properties, and the film´s response to O2 were evaluated. Results showed that annealing improves surface homogeneity and oxygen sensitivity, highlighting the role of oxygen vacancies in gas sensing

efficiency. Photoluminescence and cathodoluminescence spectra revealed that specific color centers, such as oxygen vacancies with trapped electrons, enhance the ZrO_2 surface's sensitivity to oxygen. These findings emphasize the relationship between defect structures and material performance in gas sensing applications, offering insights for optimizing ZrO_2-based sensors.

Keywords

ZrO_2 films; ALD films; Annealing; Thin film sensors

Introduction

ZrO_2 thin films have garnered significant attention in materials science due to their exceptional thermal stability, high dielectric constant, and excellent mechanical properties [1–3]. These attributes make ZrO_2 ideal for technological applications such as ferroelectrics, thermal barrier coatings, and gas-sensing devices [4–10]. Atomic layer deposition (ALD) techniques have enabled precise control over the thickness and composition of ZrO_2 films at the atomic level, enhancing their quality and performance[11].

Traditionally, ZrO_2 fabrication via ALD uses Tetrakis(dimethylamino)zirconium (TDMAZ) as a precursor and H_2O as an oxidizing agent. However, recent studies have shown that these precursors do not fully oxidize when reacting with H_2O, requiring more potent oxidizing agents such as plasma for complete oxidation [12].

High-temperature annealing is another effective technique for optimizing the structural and functional properties of ZrO_2 thin films by modifying defect structures [13]. Defects in materials are crucial for applications in catalysis, electronics, and sensing technologies. However, proper characterization and understanding of these defects and their impact on material performance remain active research areas.

In this study, we investigated the effects of annealing on the structural, optical, and gas-sensing properties of ZrO_2 thin films deposited via ALD. The films were annealed at different temperatures in an N_2 atmosphere, and their impact on surface morphology, chemical composition, and optical properties was characterized. Gas sensing evaluations were conducted to determine the film´s response to O_2, analyzing the results about surface roughness, O/Zr ratio, and oxygen vacancy defects. By studying the photoluminescence and cathodoluminescence spectra of ZrO_2 films, we aimed to better understand the electronic states and transitions associated with different types of defects and color centers, elucidating their impact on the overall material performance.

RESULTS

Spectroscopic Ellipsometry

Figure 1c-f illustrates the ellipsometry raw ψ (in blue) and Δ (in red) data and their corresponding model fits (dotted lines) for the ZrO_2 films and those annealed at 700

°C, 800 °C, and 900 °C. The Tauc-Lorentz model was used and can be expressed as follows[14]:

$$\varepsilon_2 = \frac{AE_0C(E-E_g)^2}{(E^2-E_0^2)^2+C^2E^2}\frac{1}{E}$$

for E>E_g where A is the oscillator amplitude or strength, E_0 is the energy of each oscillator, E is the incident photon energy, E_g represents the band gap, and the C parameter represents the broadening of each oscillator.

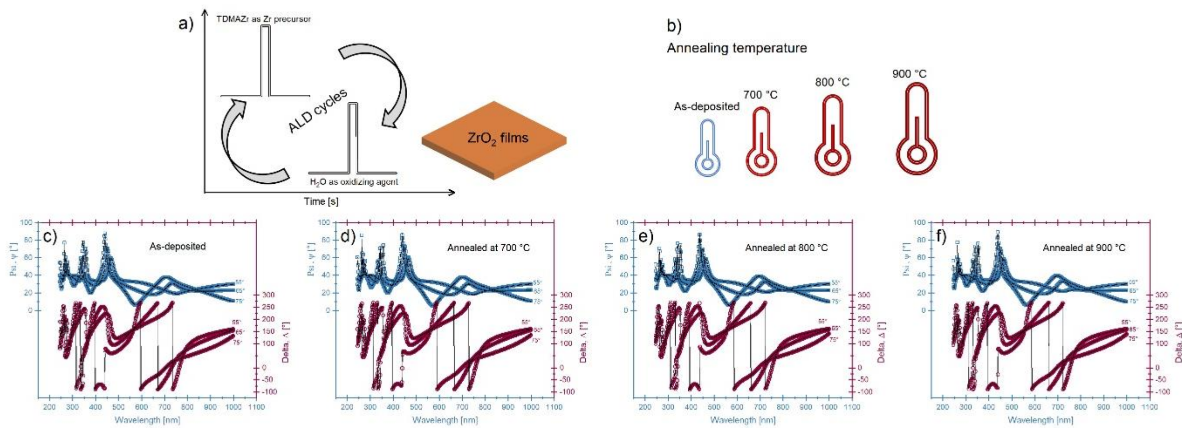

Figure 1: (a)-(b) Schematic representation of the fabrication of ZrO_2 films by atomic layer deposition (ALD) and subsequent annealing treatment. (c)-(f) Raw ellipsometry data for ψ and Δ parameters and corresponding fittings using an optical model based on the Tauc-Lorentz theory.

The extracted parameters from the model fit were the refractive index and extinction coefficient, as shown in Figure 2. Panel 2a shows how the refractive index reaches a maximum in the ZrO_2 film annealed at 700 °C. Initially, the refractive index of the as-deposited ZrO_2 film is 2.16 at a wavelength of 632 nm. Then, the value increased to 2.18 when annealed at 700 °C and then decreased to 2.14 and 2.13 for the ZrO_2

annealed at 800 °C and 900 °C, respectively. The formation of oxygen vacancies and other structural defects at these temperatures can alter the material's electronic structure, reducing its ability to polarize in response to incident light, thereby lowering the refractive index. Additionally, the refractive index measured by Synowicki and Tiwald for 2 mm thick cubic ZrO_2 crystals was included, which shows values similar to those obtained in this study[15].

Figure 2b shows the extinction coefficient, revealing a trend like the refractive index. The ZrO_2 film annealed at 700 °C shifts to longer wavelengths, and the film's absorption starts at 293 nm. The absorption curve starting at 268 nm is the as-deposited ZrO_2 film. Meanwhile, the films annealed at 800 °C and 900 °C shift towards higher energies, starting around 258 nm. Additionally, extinction coefficient values measured by Synowicki and Tiwald [15] (black line) were included, closely matching those observed for ZrO_2 films annealed at 800 °C and 900 °C.

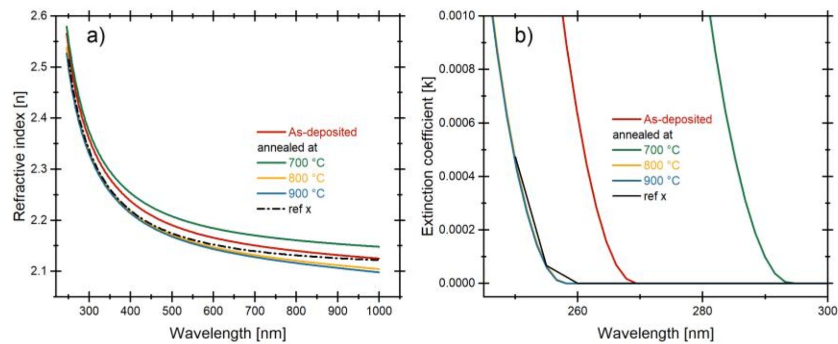

Figure 2: (a) Refractive index profiles for ZrO_2 films deposited via ALD, as-deposited and annealed at 700°C, 800°C, and 900°C, with the reference refractive index measured by Synowicki and Tiwald [15]. (b) The corresponding extinction coefficients for these films.

UV-Visible spectroscopy

To determine the bandgap energy of the ZrO_2 films, we conducted UV-Vis transmittance measurements on the samples grown on translucid sapphire. Figure 3a presents the transmittance spectra. Referenced against sapphire as 100 %, it demonstrates transparency across the visible range. However, there is a noticeable decrease in transmittance in the UV region, which can be attributed to the characteristics of the bandgap. Figure 3b shows the Tauc plot, derived from the absorption coefficient of the UV-Vis measurements while considering the film thickness determined by ellipsometry. A minimal, yet distinguishable, variation in the bandgap among the samples is observed. The as-deposited ZrO_2 exhibited a value of 5.80 eV, whereas the films annealed at 700, 800, and 900 °C showed values of 5.79, 5.81, and 5.82 eV, respectively.

The correlation between the refractive index and the bandgap energy is shown in Figure 3c. As the bandgap increases, the refractive index decreases, aligning with various empirical models proposed by multiple researchers. The Moss relation (yellow line) is derived from the Bohr atomic model and the collective oscillations of electrons. It connects the bandgap of a material to the refractive index by stating that the bandgap is inversely proportional to the fourth root of the refractive index [16]. Reddy et al. [17] (purple line) and Anani et al. [18] (blue line) proposed modifications to the Moss relation, introducing empirical adjustments to improve the correlation between the refractive index and the band gap, although with added arbitrary

constants with no specific physical meaning. Our data, graphed as squares and marked with a red dotted line, align more closely with the Moss relation. The graph shows that the static refractive index (n_0) as a function of the band gap energy for our ZrO_2 films aligns more closely with the Moss relation, represented by the yellow line than the modifications proposed by Reddy and Anani.

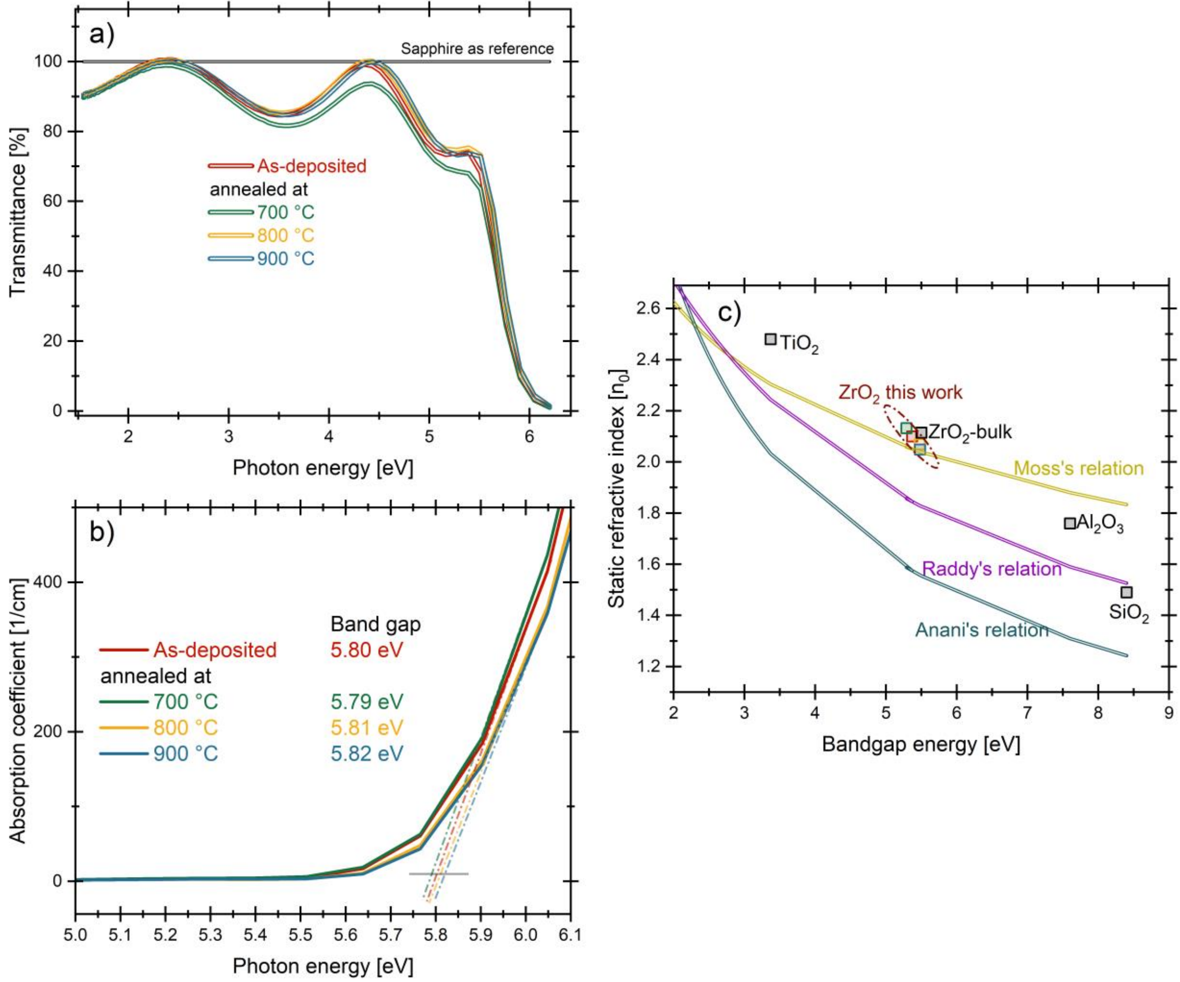

Figure 3: a) UV-Vis transmittance of the ZrO_2 films grown on the sapphire substrates, b) Tauc-plot for bandgap determination, and c) the relationship between bandgap E_g and static refractive index n_0. The graph includes the empirical

relationships proposed by Moss [16], Reddy [17], and Anani [18], along with experimental data for various metal oxides, including bulk ZrO_2 [19].

Atomic Force Microscopy

Figure 4a-d provides the 3D AFM images of the ZrO_2 films measured in 5x5 μm scan areas. The as-deposited ZrO_2 film exhibits the highest roughness value of Root Mean Square (RMS) at 3.37 nm. Further, as the annealing temperature increases, the roughness decreases. At 700°C, the roughness decreases to 1.96 nm; at 800°C, it further reduces to 1.7 nm; and at 900°C, it reaches its lowest value of 1 nm. This decrease in surface roughness indicates a smoother and more homogeneous surface, which can reduce light scattering and thus influence the refractive index. As observed in Figure 2a, the refractive index initially increases at 700°C due to densification but decreases to 800°C and 900°C, correlating with the smoother surface morphology and reduced light scattering.

Figure 4e also shows the height distribution profile derived from the AFM measurements for the four samples. This distribution could be fitted to a single Gaussian curve, signifying homogeneity. The height distribution of the deposited ZrO_2 shows an average height of about 14 nm. As the annealing temperature increased, a decrease in the average height up to 3 nm was observed. Furthermore, the distributions become noticeably narrower, demonstrating a significant improvement in the surface uniformity of the films as the annealing temperature increases.

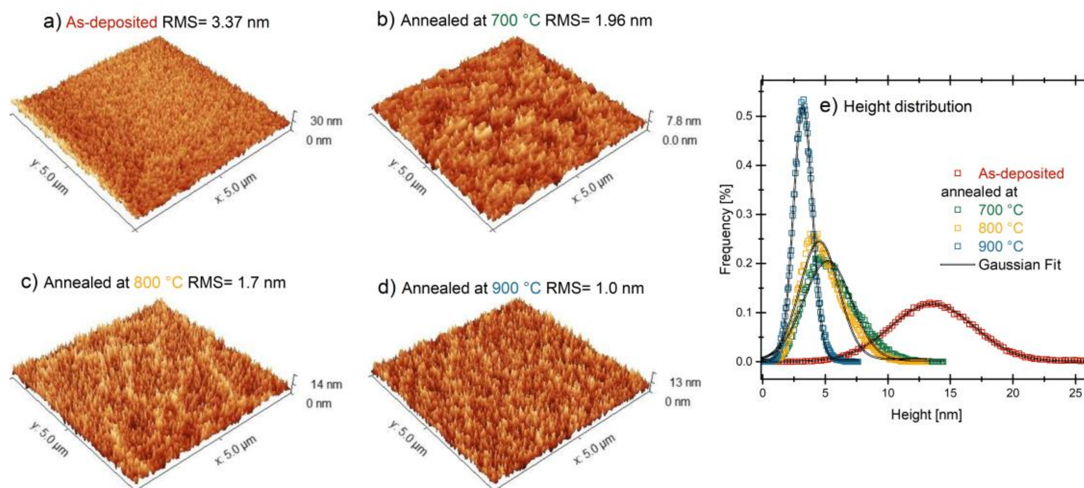

Figure 4: 3D AFM images of ZrO_2 films: (a) as-deposited and after annealing at (b) 700°C, (c) 800°C, and (d) 900°C. Panel (e) displays the height distribution of these films, with each distribution curve fitted using a Gaussian function.

X-ray Photoelectron Spectroscopy (XPS)

Figure 5a displays the high-resolution XPS Zr(3d) spectrum for the as-deposited ZrO_2 films and those annealed at 700°C, 800°C, and 900°C. The Zr($3d_{5/2}$) peak appeared at a binding energy of 182.4 eV, and the Zr($3d_{5/2}$) 3d orbital splitting was measured at 2.4 eV for all the samples, corresponding to the Zr^{+4}[20]. No additional oxidation states were observed.

On the other hand, Figure 5b presents the high-resolution XPS spectra for the O1s signal, identifying three regions. These include the O-Zr bond at ≈529.6 eV, oxygen vacancies at ≈530.6 eV, and OH groups associated with adsorbed H_2O at ≈532 eV. No significant differences were found between the Zr(3d) and O(1s) spectra after annealing, neither in the shape nor position of the peaks.

However, the O/Zr ratio increases from 1.88 for as-deposited ZrO_2 to 1.92 for ZrO_2 annealed at 900 °C, passing through 1.89 and 1.90 for ZrO_2 annealed at 700 °C and 800 °C, respectively. Although these differences do not indicate the presence of other phases or different oxidation states, they are significant because they reflect variations in the defect structure, especially in the number of oxygen vacancies, which affect the optical and gas-sensing properties of the films.

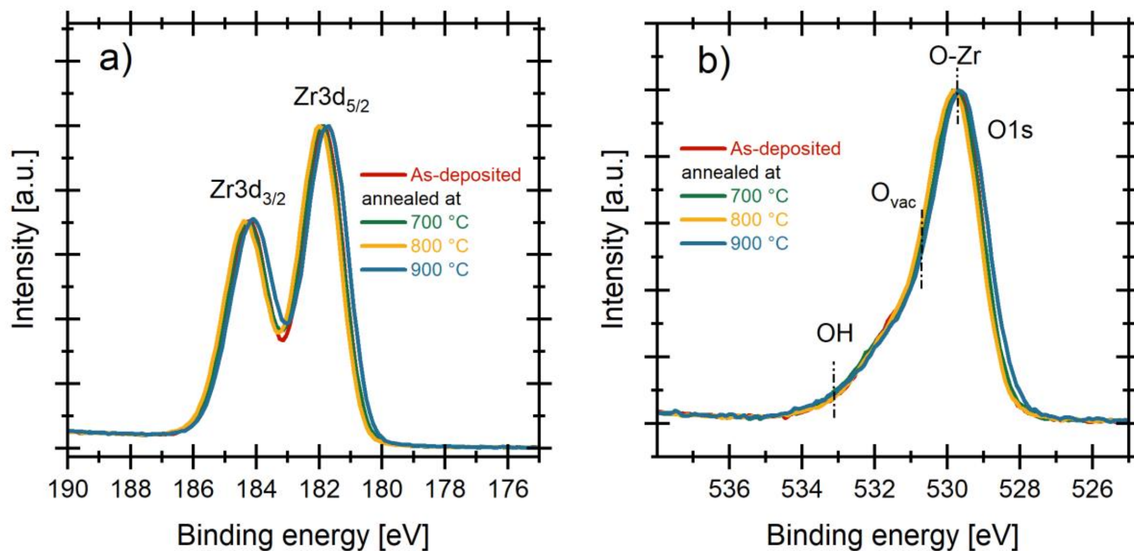

Figure 5: Comparative analysis of XPS spectra for as-deposited ZrO_2 films and those annealed at 700°C, 800°C, and 900°C. (a) presents the high-resolution Zr(3d) spectra, and (b) the high-resolution O(1s) spectra.

Cathodoluminescence and Photoluminescence

Figure 6 presents the PL spectra in blue and the CL spectra in red for the ZrO_2 films. The PL spectra consistently show lower energies than the CL spectra, attributed to the varying excitation mechanisms of each technique [21]. Consequently, Figure 7a-

d presents the deconvoluted PL spectra of the annealed ZrO_2 films to analyze their contributions. The four luminescence spectra were decomposed into 5 contributions centered at 1.7 eV, 2.0 eV, 2.4 eV, 2.88 eV, and 3.05 eV.

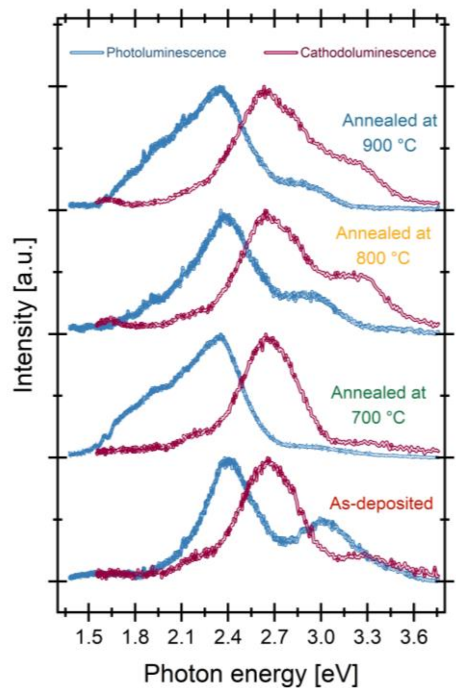

Figure 6: Photoluminescence (blue lines) and cathodoluminescence (red lines) spectra of the as-deposited ZrO_2 films and those annealed at 700°C, 800°C, and 900°C.

The 1.70 eV emission has been observed in ZrO_2 powders and is attributed to impurities present in the material, such as residual synthesis precursors and organic contaminants [22]. This peak is minimal in our case and does not undergo significant changes throughout the annealing processes, remaining almost constant in intensity and position from the as-deposited sample to the sample annealed at 900°C. This peak is rarely reported because standard PL measurements are conducted up to

600 nm. However, the emission is around 700 nm in studies extending this range. In the work of Salari et al., this emission was observed in ZrO_2 thin films between 690-700 nm with excitations at 200 nm, 246 nm, and 300 nm[23]. Additionally, in ZrO_2 nanoparticles, a PL emission centered at 660 nm has been observed[24]. This emission is not attributed to a specific material structure defect.

The emission at 2.0 eV (600 nm) is associated with the transfer of an electron from the valence band to local mid-gap states, known as the F_{AA}^{+} color center [25,26]. This center has an oxygen vacancy with two trapped electrons and a net positive charge. At 700 °C, the intensity of the 2.0 eV emission increases significantly, indicating more trap states. This increase may be due to defect rearrangement induced by the thermal treatment. The intensity decreases at 800 °C and increases again at 900 °C but does not reach the level observed at 700 °C.

The emission at 2.40 eV is associated with the F_{A}^{+} center corresponds to an electron trapped in an oxygen vacancy near a zirconium cation [25,26]. This signal undergoes a slight redshift to 2.37 eV but remains relatively stable in position and intensity during annealing at 700 °C, 800 °C, and 900 °C. This stability indicates that the thermal treatments do not significantly affect the defect. This is the most intense emission for all four samples, with only a slight decrease observed in the sample annealed at 900 °C compared to the other emissions.

The emission at 2.88 eV is attributed to oxygen vacancies that have trapped electrons, resulting in a net neutral charge associated with the *F* center. Its intensity changes with thermal treatments, significantly increasing at 800 °C. This defect is crucial for oxygen sensing because oxygen vacancies act as active sites for oxygen

molecule adsorption. These interactions change the material's electrical properties, enhancing the sensor's sensitivity and response.

The final PL peak at 3.0 eV (414 nm) is associated with Zr^{4+} vacancies and is thought to result from the recombination emissions of free excitons near the band edge (NBE) [27]. In our study, this peak's intensity decreases with annealing. It is notably strong in the as-deposited sample but decreases with thermal treatment. At 700 °C, the intensity decreases, and this reduction becomes more pronounced at 800 °C and 900 °C.

The CL spectra of the annealed ZrO_2 films, shown in Figures 7e-h, present four primary emissions. These emissions are centered at 2.30 eV, 2.67 eV, 2.85 eV, and 3.28 eV. The 2.30 eV emission is assigned to the F_A^+ center, similar to the PL emission at the same energy [25,26,28,29]. This color center involves an oxygen vacancy with a trapped electron, resulting in a net positive charge. Initially, the emission undergoes a slight redshift to 2.25 eV at 800 °C and 2.28 eV at 900 °C. Additionally, its intensity generally decreases with annealing.

The 2.67 eV emission, assigned to the singly ionized oxygen vacancy defect F^+ center, is the most intense in the as-deposited ZrO_2. At 700 °, it remains the most intense emission. It still dominates at 800 °C and 900 °C but shows a redshift to 2.65 eV. This color center involves an oxygen vacancy with a trapped electron, resulting in a positive charge [25,30].

The 2.85 eV emission is attributed to oxygen vacancies [25,31]. This emission increases with each annealing temperature conducted in an N_2 atmosphere. Oxygen vacancies are crucial for O_2 sensing as they are active sites for oxygen molecule

adsorption, enhancing the sensor's sensitivity and response. In Figure 7, this emission frows with temperature, indicating increased oxygen vacancies (F centers). This increase suggests a better sensing response as the annealing temperature rises.

The CL emission at 3.28 eV may have a similar origin to the 3.0 eV PL emission associated with Zr^{4+} vacancies [27]. This CL emission may also be linked to the recombination of free excitons near the band edge but at a slightly higher energy. The decrease in intensity with annealing suggests that thermal treatment affects Zr^{4+} vacancies and free excitons, reducing the number of these defects and thus varying the emission, with a maximum in the film treated at 800 °C, confirming the behavior observed in PL.

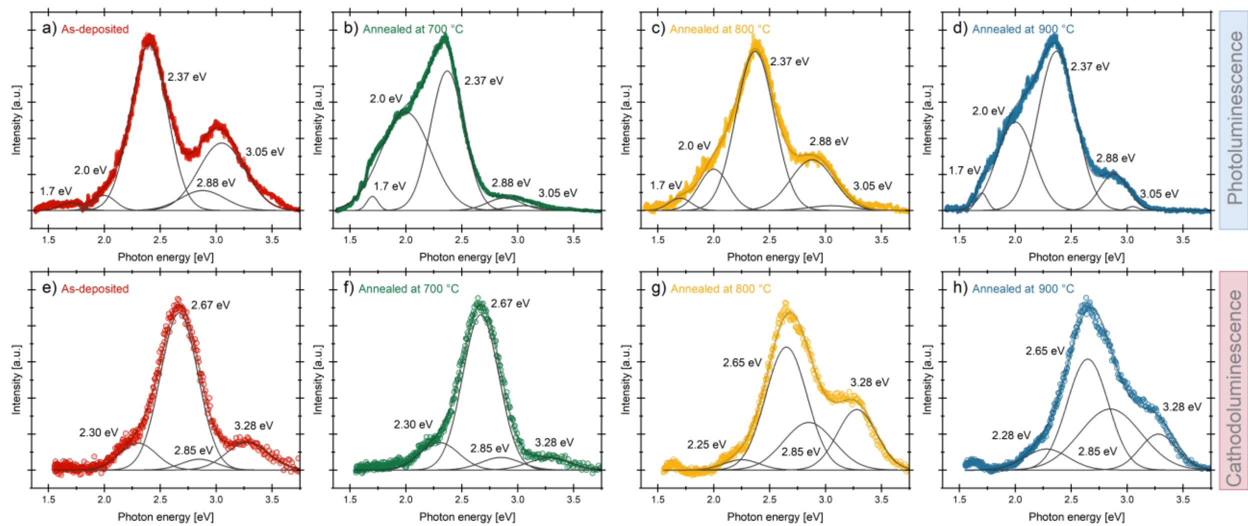

Figure 7: The deconvolutions of the cathodoluminescence spectra of the as-deposited and thermally treated ZrO_2 films are shown in (a-d). The deconvolutions of the photoluminescent spectra are shown in (e–h).

Gas sensing evaluation

The ZrO_2 sensing evaluation is presented in Figure 8. The sensor device was built on a Si substrate with a 300 nm SiO_2 layer; ZrO_2 was grown through ALD, and interdigitated Indium contacts were deposited by thermal evaporation using a shadow mask. Figure 8a-c presents a SEM micrograph of the Indium contacts, schematics, and test setup and fixture views. Figure 8d shows the potential difference (ΔV) as a function of O_2 concentration in the test chamber at 300 °C, with an operating current of 1 μA. Here, ΔV is defined as $(V_g - V_0)/V_0$, where V_g is the output voltage measured on the sensor when exposed to O_2 and V_0 is the output voltage in a pure N_2 UHP atmosphere. An increase in ΔV values was observed with rising oxygen concentration and higher annealing temperatures of the ZrO_2 films.

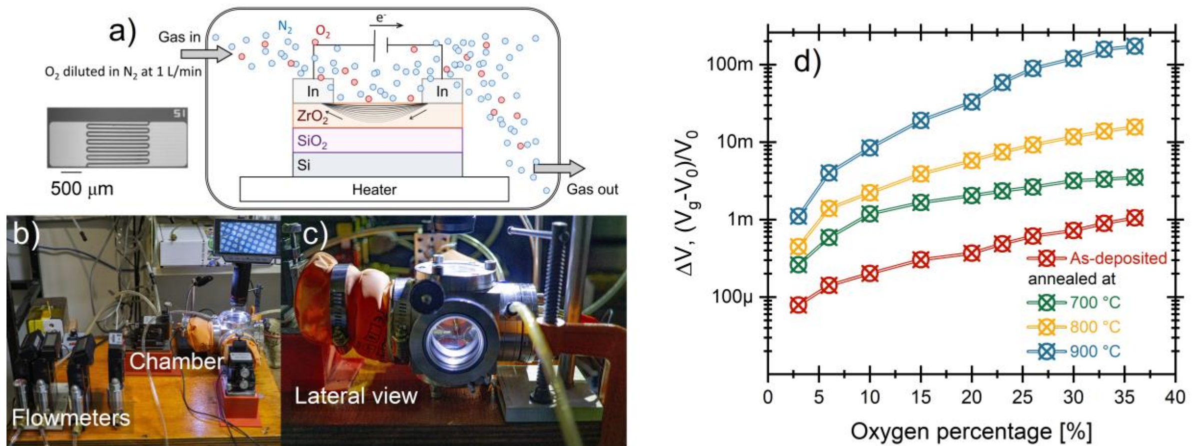

Figure 8: a) SEM micrograph of the interdigitated Indium contacts on ZrO_2 utilized for O_2-sensing measurements and a 2D drawing of the measurement setup. b) Front and c) side view of the lab-made test chamber for thin film sensor evaluations. d)

Potential difference as a function of the oxygen concentration within the chamber for the annealed ZrO_2 films at operating conditions of 300 ºC and 1 μA.

Discussion

Incorporation of O_2 in ZrO_2 films during annealing

The first point to discuss is incorporating oxygen in the ZrO_2 films during annealing. All annealing treatments were conducted in N_2 environments with less than 100 ppm of O_2, so the O/Zr ratio at the surface is not expected to increase, as confirmed by XPS measurements. However, it is believed that a higher purity level is necessary to prevent the complete incorporation of O_2.

The refractive index and bandgap results suggest that incorporating O_2 in the ZrO_2 may have affected them in several ways. Firstly, it is reasonable to consider that incorporating O_2 increases the density of the ZrO_2 lattice, thereby increasing the refractive index. However, as shown in Figure 2a, we observed a decrease in the refractive index for ZrO_2 annealed at 800 °C and 900 °C. Based on the AFM results in Figure 3, which show that the surface of ZrO_2 becomes smoother and more homogeneous, this smoother surface scatters less light, reducing the refractive index [32]. On the other hand, the bandgap values calculated from the transmittance measurements shown in Figure 3 follow the expected trend. Incorporating O_2 in ZrO_2 removes intermediate states in the bandgap, thus increasing its size.

About the gas sensing properties of ZrO_2 films

To discuss the gas-sensing properties of ZrO_2, we first plotted sensitivity versus the O/Zr ratio and surface roughness, as shown in Figure 9. The sensitivity value considered was 36% O_2 from the measurements in Figure 8. The direct relationship between sensitivity and the O/Zr ratio may seem counterintuitive, as one might expect a higher content of oxygen vacancies to provide more sites for oxygen absorption. However, considering the inverse relationship between sensitivity and roughness, the situation can be explained as follows.

Typically, higher roughness offers a larger surface area for molecules to adsorb onto film surfaces. However, Plashnitsa et al.[6] demonstrated that reducing roughness can enhance the surface selectivity of specific molecules. In their study, sensors based on YSZ with smoother and less rough surfaces exhibited better selectivity and sensitivity towards gases like NO_2 and C_3H_6. Lower roughness contributes to excellent stability and repeatability in forming catalytic active sites.

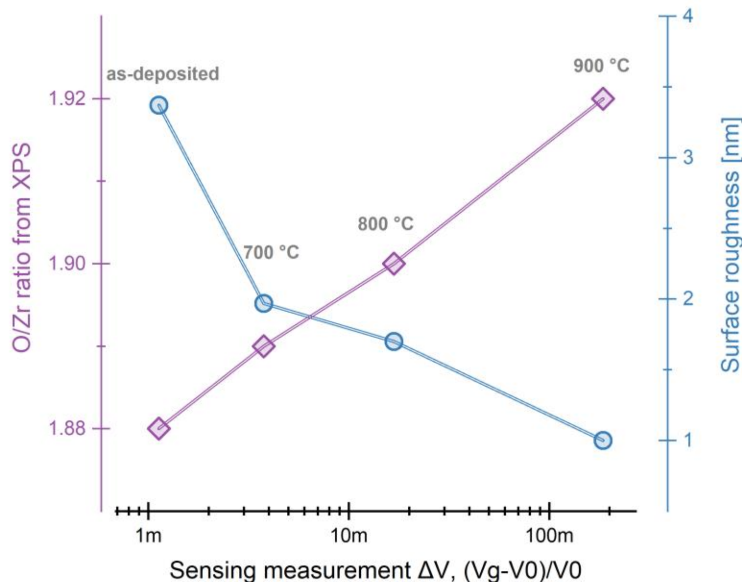

Figure 9: The O/Zr ratio and surface roughness parameters of the annealed ZrO_2 films as a function of the O_2 sensitivity ΔV measured at 36 % de O_2 at 300 ºC.

On the other hand, the summary of emissions identified by PL and CL is shown in Figure 10. When considering the variation in emissions observed with annealing, they can be linked as follows. Despite the increase in the O/Zr ratio with annealing, the temperature-induced lattice rearrangement promoted an increase in oxygen vacancies that trap electrons, as identified by PL and CL emissions at 2.85 eV and 2.88 eV. Thus, annealing appears to favor the formation of the *F* center over other defects, thereby enhancing the ZrO_2 surface sensitivity oxygen.

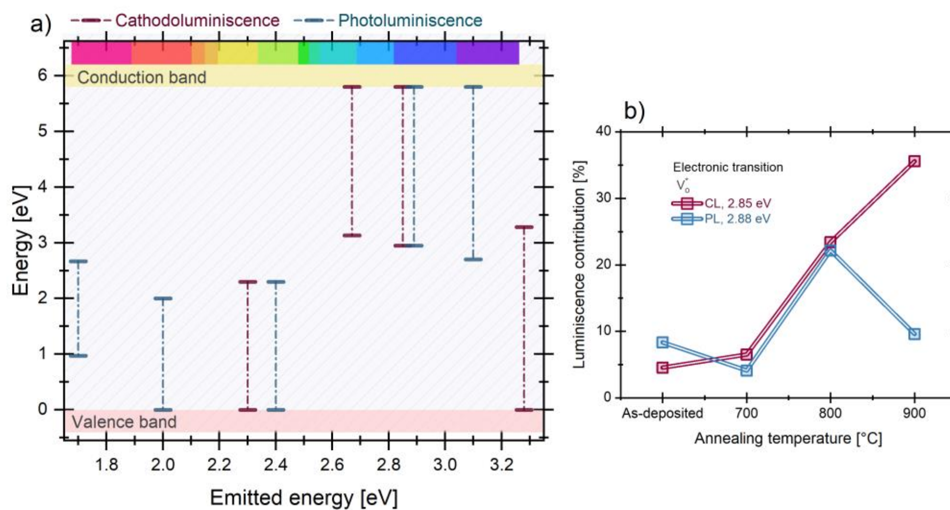

Figure 10: (a) Energy emission levels observed in Cathodoluminescence and Photoluminescence spectra. The data points represent emitted photon energies for various electronic transitions. Conduction and valence bands are indicated for reference. (b) Luminescence contribution is a function of annealing temperature for

the electronic transition at approximately 2.85 eV in CL and 2.88 eV in PL, corresponding to the oxygen vacancies.

Conclusion

Incorporating oxygen in ZrO_2 films during annealing leads to smoother and more homogeneous surfaces, which reduce light scattering and lower the refractive index. As a result, the inverse relationship between the refractive index and the bandgap aligns more closely with the Moss relation.

Contrary to the belief that higher surface roughness increases sensitivity by providing a larger adsorption area, it has been demonstrated that reduced roughness enhances the selectivity and stability of catalytic active sites. This results in greater sensitivity to specific gases such as O_2.

Despite the increase in the O/Zr ratio with annealing, the temperature-induced lattice rearrangement increases the presence of oxygen vacancy defects, as observed in emissions at 2.85 eV and 2.88 eV in PL and CL spectra. These specific *F* color centers enhance the ZrO_2 surface's sensitivity to oxygen.

Experimental

Fabrication

ZrO_2 films were deposited using the ALD method (Beneq TFS-200) at 200° C within a viscous flow reactor. The Tetrakis(ethylmethylamino)Zirconium (TEMAZr) was used as Zr precursors, and H_2O as an oxidizing agent. The substrates used were SiO_2/Si (100) and sapphire acquired from UniversityWafer (ID 1432 and 1251). The thickness of the films was ~100 nm with a growth rate of ~0.8 Å/cycle. Afterward, three annealing treatments were carried out at 700, 800, and 900 °C in an N_2 environment with ppm of O_2 less than 100 for one hour. The fabrication scheme is shown in Figure 1a-b.

Characterization

Thickness and optical constants of the ZrO_2 films were determined by Spectroscopic Ellipsometry (SE) measured at three angles of incidence, 55°, 65°, and 75°, using a J.A. Wollam M-2000 ellipsometer. The data analysis was performed using a Tauc-Lorentz model within the completeEASE software with a mean square error (MSE) of less than 10.

Surface morphology was evaluated by Atomic Force Microscopy (AFM) on a 5 µm x 5 µm area operating in a tapping mode (Park system model XE-70). Also, the surface chemical composition of the ZrO_2 films was evaluated by X-ray Photoelectron Spectroscopy (XPS) in a SPECS system with a hemispherical PHOIBOS 150 WAL analyzer. The spot size was 2 mm, and the measurements were taken with a pass energy of 20 eV and a resolution of 0.1 eV for high-resolution spectra. On the other

hand, Optical absorption characteristics were determined by UV-visible spectroscopy using an Agilent Cary 50 spectrophotometer. Measurements were taken in the 190 – 900 nm range with a resolution of 1 nm.

Cathodoluminescence (CL) and photoluminescence (PL) properties were evaluated. The CL response was excited with an electron source operated at 15 kV, and the measurements were collected with a Gatan mono-CL system in an SEM JEOL FIB-4500 system in the range of 330 to 800 nm. The PL signal was excited with a He-Cd UV laser of 325 nm in a Horiba Jobin-Yvon LabRam HR800 equipped with a confocal Raman microscope. The spectral acquisition range was 330 to 900 nm.

Finally, the gas-sensing properties of the ZrO_2 films were tested in a custom-built chamber equipped with gas flow and heating systems. The experiments involved varying the O_2 concentration to 1 L/min in ultra-high purity N_2 and evaluating the electrical response of planar devices based on ZrO_2 films at 300 °C. 50-micron interdigitated Indium contacts were thermally evaporated at $1x10^{-5}$ torr in a JEOL JEE-400 system using a commercial shadow mask by Ossila. Electrical measurements were acquired using a Source Meter unit, Keithley 2450.

Acknowledgments

The authors acknowledge the financial support by DGAPA-UNAM Grants No. IN110424 and IN119023. FORDECYT Grants No. 21077; and FONCICyT Grant No. 246648.

The authors acknowledge the technical support of J.A. Díaz, I. Gradilla, E. Aparicio, E. Murillo, L. Arce, and D. Domínguez.

References

(1) Patil, R. N.; Subbarao, E. C. *urn:issn:0021-8898* **1969**, *2*, 281–288. doi:10.1107/S0021889869007217

(2) Mahajan, A. M.; Khairnar, A. G.; Thibeault, B. J. *Silicon* **2016**, *8*, 345–350. doi:10.1007/S12633-015-9322-7/METRICS

(3) Ravi Kumar, K.; Pridhar, T.; Sree Balaji, V. S. *J Alloys Compd* **2018**, *765*, 171–179. doi:10.1016/J.JALLCOM.2018.06.177

(4) Panda, D.; Tseng, T. Y. *Thin Solid Films* **2013**, *531*, 1–20. doi:10.1016/J.TSF.2013.01.004

(5) Lin, B. T.; Lu, Y. W.; Shieh, J.; Chen, M. J. *J Eur Ceram Soc* **2017**, *37*, 1135–1139. doi:10.1016/J.JEURCERAMSOC.2016.10.028

(6) Plashnitsa, V. V.; Elumalai, P.; Fujio, Y.; Miura, N. *Electrochim Acta* **2009**, *54*, 6099–6106. doi:10.1016/J.ELECTACTA.2008.12.040

(7) Schulz, U.; Schmücker, M. *Materials Science and Engineering: A* **2000**, *276*, 1–8. doi:10.1016/S0921-5093(99)00576-6

(8) Mohammed, M. A.; Razaq, S. . doi:10.14704/nq.2020.18.3.NQ20146

(9) Lou, C.; Li, Z.; Yang, C.; Liu, X.; Zheng, W.; Zhang, J. *Sens Actuators B Chem* **2021**, *333*, 129572. doi:10.1016/J.SNB.2021.129572

(10) Mokrushin, A. S.; Simonenko, E. P.; Simonenko, N. P.; Bukunov, K. A.; Sevastyanov, V. G.; Kuznetsov, N. T. *J Alloys Compd* **2019**, *773*, 1023–1032. doi:10.1016/J.JALLCOM.2018.09.274

(11) Cassir, M.; Goubin, F.; Bernay, C.; Vernoux, P.; Lincot, D. *Appl Surf Sci* **2002**, *193*, 120–128. doi:10.1016/S0169-4332(02)00247-7

(12) Cho, G. Y.; Noh, S.; Lee, Y. H.; Ji, S.; Hong, S. W.; Koo, B.; An, J.; Kim, Y.-B.; Cha, S. W. *Journal of Vacuum Science & Technology A: Vacuum, Surfaces, and Films* **2016**, *34*. doi:10.1116/1.4938105/246543

(13) Abbas, Y.; Han, I. S.; Sokolov, A. S.; Jeon, Y. R.; Choi, C. *Journal of Materials Science: Materials in Electronics* **2020**, *31*, 903–909. doi:10.1007/S10854-019-02598-X/FIGURES/4

(14) Jellison, G. E. *Thin Solid Films* **1998**, *313–314*, 33–39. doi:10.1016/S0040-6090(97)00765-7

(15) Synowicki, R. A.; Tiwald, T. E. *Thin Solid Films* **2004**, *455–456*, 248–255. doi:10.1016/J.TSF.2004.02.028

(16) Moss, T. S. *physica status solidi (b)* **1985**, *131*, 415–427. doi:10.1002/PSSB.2221310202

(17) Reddy, R. R.; Nazeer Ahammed, Y.; Rama Gopal, K.; Raghuram, D. V. *Opt Mater (Amst)* **1998**, *10*, 95–100. doi:10.1016/S0925-3467(97)00171-7

(18) Anani, M.; Mathieu, C.; Lebid, S.; Amar, Y.; Chama, Z.; Abid, H. *Comput Mater Sci* **2008**, *41*, 570–575. doi:10.1016/J.COMMATSCI.2007.05.023

(19) Gomaa, H. M.; Yahia, I. S.; Zahran, H. Y. *Physica B Condens Matter* **2021**, *620*, 413246. doi:10.1016/J.PHYSB.2021.413246

(20) Matsuoka, M.; Isotani, S.; Sucasaire, W.; Kuratani, N.; Ogata, K. **2007**. doi:10.1016/j.surfcoat.2007.11.019

(21) Pelant, I.; Valenta, J. *Luminescence Spectroscopy of Semiconductors* **2012**, *9780199588336*, 1–560. doi:10.1093/ACPROF:OSO/9780199588336.001.0001

(22) Boffelli, M.; Zhu, W.; Back, M.; Sponchia, G.; Francese, T.; Riello, P.; Benedetti, A.; Pezzotti, G. **2014**. doi:10.1021/jp506923p

(23) Salari, S.; Ghodsi, F. E. *J Lumin* **2017**, *182*, 289–299. doi:10.1016/J.JLUMIN.2016.10.035

(24) Sagadevan, S.; Podder, J.; Das, I. *Journal of Materials Science: Materials in Electronics* **2016**, *27*, 5622–5627. doi:10.1007/S10854-016-4469-6/FIGURES/10

(25) Vokhmintsev, A. S.; Petrenyov, I. A.; Kamalov, R. V.; Karabanalov, M. S.; Weinstein, I. A. *J Lumin* **2022**, *252*, 119412. doi:10.1016/J.JLUMIN.2022.119412

(26) Pezzotti, G.; Munisso, M. C.; Porporati, A. A.; Lessnau, K. *Biomaterials* **2010**, *31*, 6901–6908. doi:10.1016/J.BIOMATERIALS.2010.05.035

(27) Méndez-López, A.; Zelaya-ángel, O.; Toledano-Ayala, M.; Torres-Pacheco, I.; Pérez-Robles, J. F.; Acosta-Silva, Y. J. *Crystals 2020, Vol. 10, Page 454* **2020**, *10*, 454. doi:10.3390/CRYST10060454

(28) Leto, A.; De Portu, G.; Mercadelli, E.; Sanson, A.; Pezzotti, G. *Ceram Int* **2015**, *41*, 2247–2252. doi:10.1016/J.CERAMINT.2014.10.027

(29) Boffelli, M.; Zhu, W.; Back, M.; Sponchia, G.; Francese, T.; Riello, P.; Benedetti, A.; Pezzotti, G. *Journal of Physical Chemistry A* **2014**, *118*, 9828–9836. doi:10.1021/JP506923P/ASSET/IMAGES/MEDIUM/JP-2014-06923P_0010.GIF

(30) Lokesha, H. S.; Nagabhushana, K. R.; Singh, F.; Tatumi, S. H.; Prinsloo, A. R. E.; Sheppard, C. J. *Journal of Physical Chemistry C* **2021**, *125*, 27106–27117. doi:10.1021/ACS.JPCC.1C07365/ASSET/IMAGES/LARGE/JP1C07365_0015.JPEG

(31) Islamov, D. R.; Gritsenko, V. A.; Perevalov, T. V.; Yelisseyev, A. P.; Pustovarov, V. A.; Korolkov, I. V.; Lomonova, E. E. *Materialia (Oxf)* **2021**, *15*, 100979. doi:10.1016/J.MTLA.2020.100979

(32) Zhu, L.; He, G.; Lv, J.; Fortunato, E.; Martins, R. *RSC Adv* **2018**, *8*, 16788–16799. doi:10.1039/C8RA02108B